Electrochimica Acta 283 (2018) 1534–1542

Contents lists available at ScienceDirect

Electrochimica Acta

journal homepage: www.elsevier.com/locate/electacta

Hydrostatic pressure effects on hydrogen entry into A514 steel with cathodic deposits

X.L. Xiong [a], Y. Xiang [a], J.X. Li [a], Y.J. Su [a, *], Q.J. Zhou [b], Alex A. Volinsky [c]

[a] Corrosion and Protection Center, Key Laboratory for Environmental Fracture (MOE), University of Science and Technology Beijing, Beijing 100083, China
[b] Research Institute, Baoshan Iron & Steel Co. Ltd, Shanghai 201900, China
[c] Department of Mechanical Engineering, University of South Florida, Tampa FL 33620, USA

ARTICLE INFO

Article history:
Received 18 February 2018
Received in revised form
2 July 2018
Accepted 10 July 2018
Available online 21 July 2018

Keywords:
Hydrogen permeation
Hydrostatic pressure
Electrochemical impedance
Deposits
FIB

ABSTRACT

Hydrostatic pressure effects on cathodic deposits and long-term hydrogen permeation in 0.2 mol/L NaOH, 3.5% NaCl and artificial seawater were characterized by the high-pressure Devanathan cell hydrogen permeation tests, electrochemical impedance spectroscopy, Raman spectroscopy, scanning electron microscopy, coupled focused ion beam lithography and energy dispersive X-ray spectroscopy. Hydrostatic pressure accelerates the hydrogen evolution reaction and causes hydrogen atoms to permeate into steel. Furthermore, hydrostatic pressure increases the interfacial pH; changes deposits from a mixture of brucite, aragonite, and calcite to brucite only; and inhibits hydrogen permeation into steel in artificial seawater. These competitive effects control the mechanisms of hydrogen entry into steel in deep seawater.

Published by Elsevier Ltd.

1. Introduction

Hydrogen-induced cracking (HIC) of super duplex stainless steel hubs and fillet weld toes in the subsea environment have been reported by several researchers [1,2]. Thus, the studies of the deep sea hydrostatic pressure effects on the hydrogen permeation kinetics have been performed. Based on the double cell hydrogen permeation tests, Nanis and DeLuccia [3], Woodward and Procter [4] claimed that hydrostatic pressure increased the permeation flux, whereas Blundy and Shreir [5], Smirnova and Johnsen [6] found that the permeation flux was independent of the hydrostatic pressure when stirring an electrolyte in a hydrogen charging cell during permeation. Obviously, electrolyte stirring affects the hydrogen evolution reaction (HER) on the hydrogen charging side of specimens in permeation tests. These experimental results indicate that the HER dominates the effects of pressure on the interaction of hydrogen with metal. The HER process of iron or steel in an alkaline solution can be described by the Volmer reaction [7–9]:

$$H_2O + M + e^- \xrightarrow{k_1} MH_{ads} + OH^- \quad (1)$$

where M is the electrode, e.g., iron or steel and MH_{ads} is the adsorbed hydrogen atom on the electrode surface. The second step is the Heyrovsky reaction:

$$MH_{ads} + H_2O + e^- \xrightarrow{k_2} H_2 + OH^- + M \quad (2)$$

The Heyrovsky reaction is coupled with the Tafel recombination:

$$MH_{ads} + MH_{ads} \xrightarrow{k_3} H_2 + 2M \quad (3)$$

In equations (1)–(3), k_1, k_2, and k_3 are the corresponding kinetic parameters of the Vollmer, Heyrovsky, and Tafel reactions. Some of the adsorbed hydrogen atoms diffuse into the subsurface just below the electrode surface and become absorbed hydrogen atoms:

$$MH_{ads} + M_{subsurface} \leftrightarrow M_{surface} + MH_{abs}(subsurface) \quad (4)$$

Then, the absorbed hydrogen atoms diffuse into metal:

$$MH_{abs}(subsurface) \rightarrow MH_{abs}(bulk) \quad (5)$$

Zhang developed a mathematical model to describe the effects of hydrogen adsorption and desorption on hydrogen permeation

* Corresponding author.
E-mail address: yjsu@ustb.edu.cn (Y.J. Su).

https://doi.org/10.1016/j.electacta.2018.07.049
0013-4686/Published by Elsevier Ltd.

[10]. Based on this model, previous work found that hydrostatic pressure increased the subsurface hydrogen concentration on the A514 steel membrane [11]. Additionally, cathodic potentiostatic hydrogen permeation tests of the A514 steel membrane specimens were performed in 0.2 mol/L NaOH under different hydrostatic pressures [12]. Once hydrogen permeation reached steady state, electrochemical impedance spectroscopy (EIS) analysis was conducted on the specimens' hydrogen charging side under the same cathodic potential. By fitting the EIS experimental data to the EIS model, which established the relationships between the kinetic parameters of HER and the impedance components in the equivalent circuit, it was demonstrated that hydrostatic pressure increased the kinetic parameter of the Volmer reaction, k_1, and decreased the kinetic parameter of the Tafel recombination, k_3. Both of these effects increased the amount of adsorbed hydrogen atoms. Furthermore, pressure increased the kinetic parameter of the Heyrovsky reaction, k_2, thus decreasing the number of adsorbed hydrogen atoms [12,13].

However, to prevent sample surface damage, the effect of pressure on the hydrogen permeation kinetics was examined over a relatively short experimental time. During long-term permeation in an alkaline solution, Zakroczymski and Flis [14] noted for the first time that the hydrogen atoms produced by cathodic polarization reduced oxidation film formation and activated the iron sample in 0.1 M NaOH. The permeation flux increased with time under these conditions. The hydrogen atoms then disintegrated the superficial metal layer. Metal particles from the metal surface became corrosion products ($Fe(OH)_2$, magnetite and hydrated Fe(III) oxides) and were deposited on the surface, inhibiting further entry of hydrogen [14–16]. In acidic solutions, cathodic polarization continually activated the iron sample surface [17]. In artificial seawater, more complex cathodic deposits were detected. In addition, the formation of calcareous deposits is related to the applied cathodic potential and interfacial pH. The OH^- groups produced in the Volmer reaction (1) and the Heyrovsky reaction (2) react with magnesium ions in seawater when the interfacial pH is higher than 9.3 [18]:

$$2OH^- + Mg^{2+} \rightarrow Mg(OH)_2\downarrow \quad (6)$$

Additionally, these reactions lead to a change in the inorganic carbonic equilibrium at the electrode surface:

$$OH^- + HCO_3^- \rightarrow H_2O + CO_3^{2-} \quad (7)$$

Calcium ions react with CO_3^{2-}:

$$CO_3^{2-} + Ca^{2+} \rightarrow CaCO_3\downarrow \quad (8)$$

Gao noted that the calcareous deposits on the 16Mn steel inhibited HER [19], while Okstad reported that the calcareous deposits on carbon steel specimens catalyzed HER [20]. Even though different opinions have been expressed regarding this problem, the effects of hydrostatic pressure on the formation of calcareous deposits should be considered when describing the pressure effects on hydrogen permeation in seawater.

Based on the Tafel plots at different hydrostatic pressures obtained in an earlier work and shown in Fig. 1 [12,21], it was found that hydrostatic pressure increased the corrosion potential of the A514 steel in 0.2 mol/L NaOH, which means that the applied overpotential was more negative under the same cathodic potential and higher hydrostatic pressure. Thus, hydrostatic pressure affects the applied overpotential. On the other hand, Deslouis et al. [22] noted that the interfacial pH depends on the applied potential because more OH^- groups were produced at a more negative cathodic potential. The pH values at the surface of the gold electrode in 0.5 M K_2SO_4 at applied potentials of −0.5 V_{SCE} and −1.0 V_{SCE} are close to 9.3 and 9.6, respectively. Additionally, the cathodic deposits on the metal surface, namely, the oxidation products in an alkaline solution [14] and calcareous deposits in seawater [18,23,24], are related to the interfacial pH during cathodic polarization. It is obvious that hydrostatic pressure, cathodic potential, interfacial pH and cathodic polarization are coupled factors that can affect the hydrogen permeation kinetics.

The aim of this work is to determine the effects of pressure on cathodic deposits and identify the coupling mechanisms of pressure and deposits with hydrogen permeation. Long-term hydrogen permeation experiments and EIS measurements on the hydrogen entry side were performed to detect the influence of cathodic deposits on hydrogen permeation under different hydrostatic pressures with different electrolytes. Scanning electron microscopy (SEM) and Raman spectroscopy were used to characterize the surface of the deposits. To observe the effects of pressure on the chemical composition of a cross-section of deposits, coupled focused ion beam lithography (FIB) and energy dispersive X-ray spectroscopy (EDS) were used.

2. Experimental

2.1. Test materials

The A514 offshore structural steel was used in this research, and its composition was as follows (wt%): 0.2 C, 0.78 Mn, 0.49 Cr, 0.20 Mo, 0.049 V, 0.0006 B, 0.0080 P, 0.006 S, and 0.020 Ti. The samples had a circular shape with a diameter and thickness of 1.2 cm and 0.5 mm, respectively, with 0.01 mm measurement error. Both sides of the specimens were polished, and one side of each specimen was coated with 100 nm of nickel via sputter deposition. This procedure was conducted using a thin film sputtering system (LAD18, KJLC).

2.2. Hydrostatic pressure test equipment

The hydrostatic pressure test equipment consisted of a two-compartment autoclave integrated with a hydraulic system and a temperature control system, as described in the previous study [11]. The temperature in the autoclave was controlled over the 0–40 °C range. The electrolyte in the autoclave can be pressurized to the maximum hydrostatic pressure of 56 MPa with a solution supplied from an external tank.

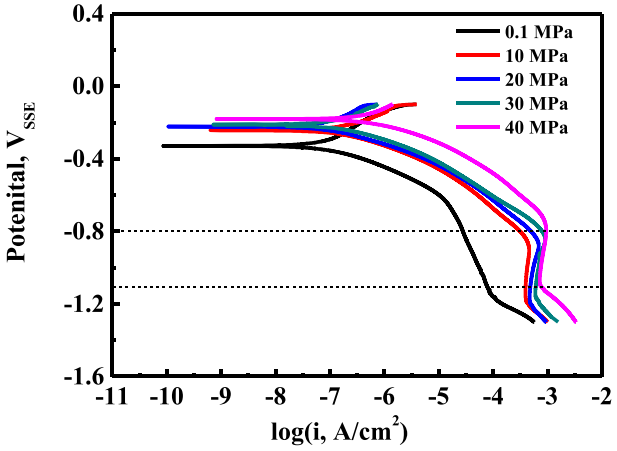

Fig. 1. Potentiodynamic polarization measurements under different hydrostatic pressures in 0.2 mol/L NaOH at 25 °C (scan rate: 0.33 mV/s, scan range: −0.1 to −1.3 V_{SSE}). Dashed lines represent the potential region with abnormal phenomena [12,21].

2.3. Electrochemical characterization

Hydrogen permeation and EIS measurements were performed using the hydrostatic pressure equipment and a three-electrode system. The counter electrode was 10 mm × 30 mm platinum sheet, while the reference electrode was Ag/AgCl electrode (+0.197 V with respect to the NHE and saturated with KCl). Test pressures of 0.1 and 30 MPa were used, which are equivalent to the hydrostatic pressure at the surface and a depth of 3000 m of the ocean. In this work, we focused on the pressure effects on hydrogen permeation and the formation of cathodic deposits. The temperature was kept at 25 °C. The temperature effects on hydrogen permeation and cathodic deposits have been widely studied. For example, for hydrogen permeation of iron, Addach et al. claimed that the steady-state current density and apparent hydrogen diffusivity in iron increased with temperature [25]. For the influence of temperature on the formation of calcareous deposits, Barchiche et al. claimed that the effects of temperature depend on the potential applied to the steel electrode. Temperature can favor aragonite at moderate cathodic potentials (e.g. −1.0 V/SCE), where the solubility of $CaCO_3$ governs the phenomenon, while it can favor brucite at more cathodic potentials (e.g. −1.2 V/SCE), where the interfacial pH, i.e. hydrogen evolution, mainly controls the deposits [26]. Thus, we didn't consider the influence of the temperature in this work.

A constant cathodic potential of −1.2 V was applied to the specimens in the hydrogen charging cell for the hydrogen permeation tests. Hydrogen atoms were produced and adsorbed onto the specimen surface, with some becoming absorbed and diffusing into the material. In the other cell (oxidation cell), a positive overpotential of +300 mV was applied to the opposite surface of the specimen. Hydrogen reaching the surface via diffusion through the specimen was immediately oxidized, and the hydrogen current was measured. In the oxidation cell, the specimen was exposed to the 0.2 mol/L NaOH electrolyte solution. In the hydrogen charging cell, 0.2 mol/L NaOH, 3.5% NaCl and the artificial seawater electrolytes described in the ASTM D1141-98 were used under different experimental conditions [27]. The composition of the artificial seawater is shown in Table 1. The pH of the artificial seawater was adjusted to 8.2 using a 0.1 M NaOH solution.

Once hydrogen permeation reached a steady state, the electrochemical workstation (Gamry Interface 1000) test mode of the hydrogen charging entry side was changed from potentiostatic polarization for hydrogen charging to EIS analysis. An AC signal with an amplitude of 10 mV was applied at a DC potential of −1.2 V. The frequency ranged from 10^5 to 0.1 Hz (from high to low). After EIS analysis was finished, the test mode was changed back to potentiostatic polarization for hydrogen charging, and hydrogen permeation tests were continued.

2.4. Deposits characterization

The sample surface morphological analysis was performed using the Zeiss Auriga SEM instrument. FIB was used to study the cross-section of the deposits. Semi-qualitative microanalysis of the cross sections was performed using EDS. Raman spectroscopy was used to identify the calcium carbonate allotropic and magnesium forms on the surface of the deposits with LabRAM HR.

Table 1
The composition of the artificial sea water.

	Composition, mol/L
NaCl	0.42
$MgCl_2$	5.46×10^{-2}
Na_2SO_4	2.80×10^{-2}
$CaCl_2$	1.05×10^{-2}
KCl	9.30×10^{-3}
$NaHCO_3$	2.80×10^{-2}

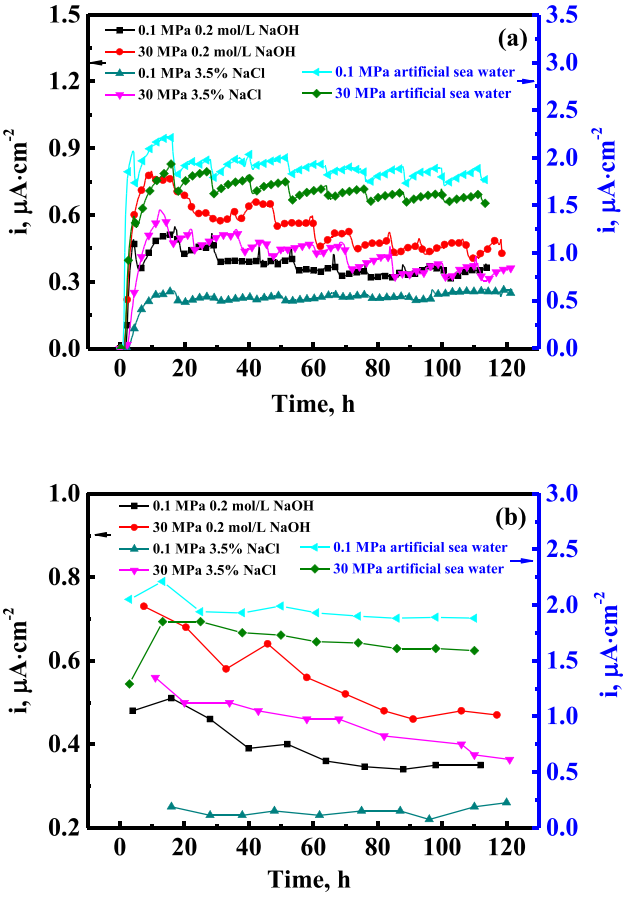

Fig. 2. (a) Long-term hydrogen permeation curves in different hydrogen charging electrolytes and under different hydrostatic pressures. (b) Steady-state current density obtained from (a).

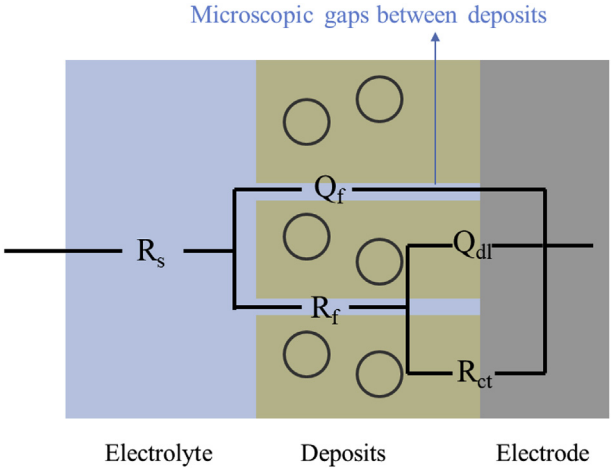

Fig. 3. Electrochemical equivalent circuits used to fit the measured EIS data, where R_s is the solution resistance; R_f and Q_f are the resistance and a constant-phase element of the cathodic deposits, respectively; and R_{ct} and Q_{dl} are the charge-transfer resistance and a constant-phase element of the double-charge layer, respectively.

3. Results

3.1. Long-term hydrogen permeation with cathodic deposits under different hydrostatic pressures

Permeation curves are shown in Fig. 2a. Fluctuations in the permeation curves were caused by the electrochemical workstation test mode changed from potentiostatic polarization to EIS analysis, as mentioned in Section 2.3.

As observed, a 30 MPa hydrostatic pressure induced a higher current density in both 0.2 mol/L NaOH and 3.5% NaCl electrolytes, corresponding to previous research results [3,4,11,12]. However, hydrostatic pressure decreased the current density in artificial seawater. To confirm that this phenomenon was not an artifact, permeation tests in artificial seawater were conducted twice under each hydrostatic pressure.

To generate more clear permeation curves, the current density data presented in Fig. 2b were obtained immediately before the EIS

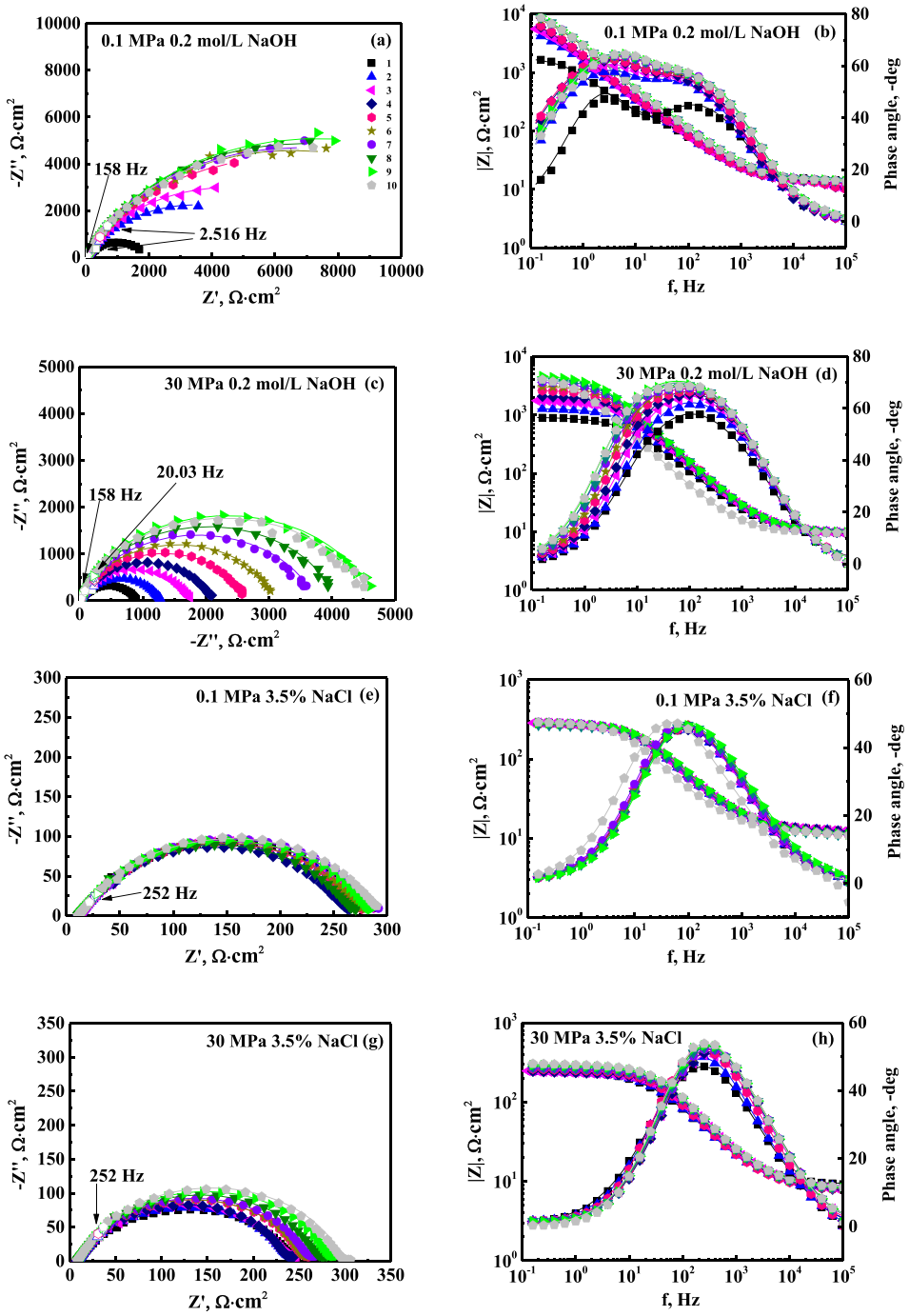

Fig. 4. The Nyquist diagrams and the Bode plots of the A514 steel specimen as a function of the test order under varied conditions (a, b) in 0.2 mol/L NaOH at 0.1 MPa, (c, d) in 0.2 mol/L NaOH at 30 MPa, (e, f) in 3.5% NaCl at 0.1 MPa, (g, h) in 3.5% NaCl at 30 MPa, (i, j) in artificial seawater at 0.1 MPa, (k, l) in artificial seawater at 30 MPa. All of the lines are the fitting results.

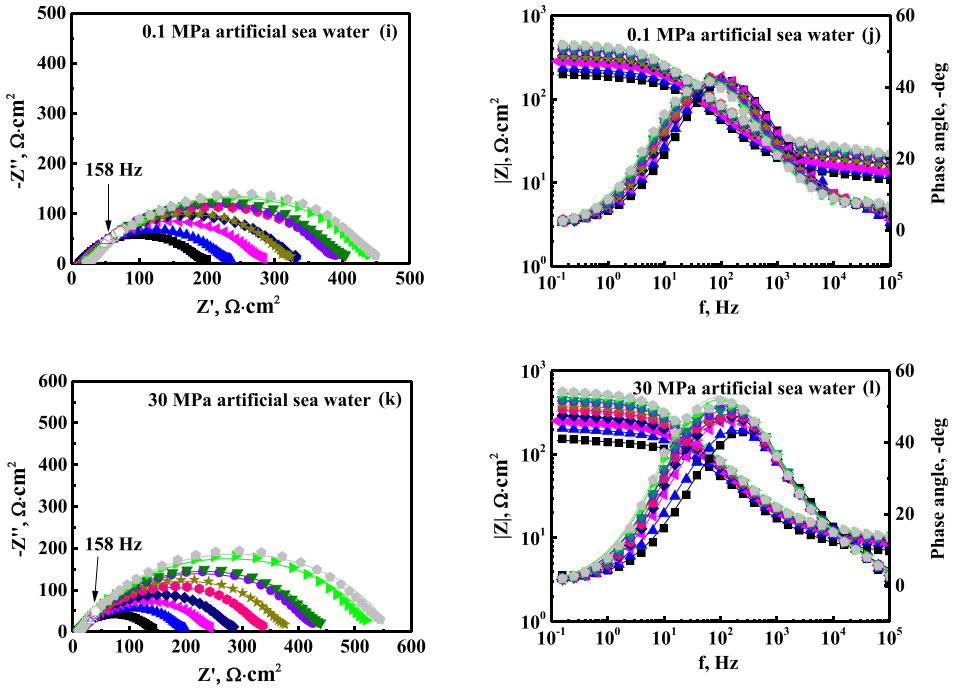

Fig. 4. (*continued*).

analysis. The permeation curves in 0.2 mol/L NaOH reached the maximum values at approximately 10 h and then slowly decreased, showing the same trend as the long-term permeation results obtained by Zakroczymski and Flis [14]. However, the decay of the current density with permeation time in 3.5% NaCl at 0.1 MPa was not obvious.

3.2. EIS analysis during permeation

EIS analysis was performed under each experimental condition during the permeation tests at certain intervals. The Nyquist diagrams and the Bode plots for the specimens under each experimental condition as a function of the testing time are shown in Fig. 4. The fitting results, shown as solid lines in Fig. 4, were obtained using the electric equivalent circuit (EEC) shown in Fig. 3. After long-term hydrogen permeation in 0.2 mol/L NaOH and 3.5% NaCl, the hydrogen entry side of the specimens was covered with brown cathodic deposits, as was also observed by Zakroczymski and Flis [14–16]. Specifically, calcareous deposits were observed on the hydrogen entry side after the hydrogen permeation tests, meaning that HER on the hydrogen entry side of the specimens, which is associated with charge transfer, occurs at the microscopic gaps in the cathodic deposits. Thus, an electrical equivalent circuit was designed, as shown in Fig. 3, where R_s, R_{ct}, R_f, Q_{dl}, and Q_f are the solution resistance, charge transfer resistance, cathodic deposit resistance, constant phase element of the double layer and constant phase element of the deposits or corrosion products, respectively. The constant-phase element, Q, rather than capacitance, was used to fit the impedance data due to the heterogeneity of the specimen surface resulted from cathodic deposits. The fitting results are shown in Table 2 and Fig. 5.

As seen in Fig. 4, the obtained Nyquist plots had flattened capacitive loops. The size of the loops increased with time, the cathodic deposits grew and the current density decreased. The trend of the impedance increasing with the permeation time was more significant in 0.2 mol/L NaOH than in 3.5% NaCl. Additionally, the size of the loop in 0.2 mol/L NaOH decreased with hydrostatic pressure, in agreement with previous work [12]. This phenomenon was also found in the 3.5% NaCl solution. Nevertheless, in artificial seawater, the size of the loop increased with hydrostatic pressure.

3.3. Deposits characterization

The morphology of the cathodic deposits in artificial seawater at −1.2 V under 0.1 and 30 MPa is shown in Fig. 6 (a) and 6(c), respectively. The deposits that formed under 0.1 MPa had more convex parts than those formed under 30 MPa. Both the convex part (1) and flat part (2) were characterized by the Raman spectroscopy. The results under 0.1 and 30 MPa are shown in Fig. 6(b) and (d).

For the deposits that formed at 0.1 MPa, the Raman spectra of the convex area (1) and flat areas (2) of the deposits (Fig. 6 (a)) showed the characteristic peaks of aragonite and calcite ($CaCO_3$, 152, 155, 204, 702, 706 and 1085 cm^{-1} wavenumbers). Additionally, brucite, $Mg(OH)_2$, was identified according to the peaks at 444, 442 and 3650 cm^{-1}, which are associated with OH^- vibrations. Barchiche et al. [24] and Héla et al. [28] also reported that a mixture of $CaCO_3$ and $Mg(OH)_2$ appeared in deposits formed under similar conditions. Thus, it is observed that some calcite was covered with aragonite and brucite and some calcite was exposed in the solution.

For the deposits formed under 30 MPa pressure, the Raman spectra at the convex area (1) showed the characteristic peaks of brucite, aragonite, and calcite. However, only brucite was detected in the flat section (2).

To observe the deposits in more detail, FIB was used to obtain the deposits' cross-section. The morphology of the cross-section of the deposits formed under 0.1 and 30 MPa is shown in Fig. 7(a) and (c). The deposits that formed under 0.1 MPa pressure were approximately 10 μm thick, while the deposits that formed under 30 MPa pressure were approximately 20 μm thick. EDS line scans of the deposits that formed under 0.1 and 30 MPa are shown in Fig. 7(b) and (d), respectively. Both Mg and Ca were detected in the

Table 2
Parameters of EIS under different hydrostatic pressure at 25 °C.

Experimental condition	Test Order	R_s Ω cm^2	R_f Ω cm^2	Q_f		R_{ct} Ω cm^2	Q_{dl}	
				Y_0, S cm^{-2}s^n	n		Y_0, S cm^{-2}s^n	n
0.2 mol/L NaOH 0.1 MPa	1	13.89	16.12	1.34×10^{-4}	0.70	3390.45	1.12×10^{-4}	0.92
	2	12.66	23.25	1.42×10^{-4}	0.70	8619.80	1.63×10^{-5}	0.93
	3	12.4	29.36	1.24×10^{-4}	0.71	1.05×10^{4}	1.34×10^{-5}	0.96
	4	12.49	28.47	1.16×10^{-4}	0.72	1.19×10^{4}	1.07×10^{-5}	0.94
	5	12.36	35.20	1.13×10^{-4}	0.72	1.27×10^{4}	1.04×10^{-5}	0.92
	6	13.85	35.00	6.25×10^{-5}	0.76	1.34×10^{4}	1.71×10^{-5}	0.92
	7	13.93	46.00	6.60×10^{-5}	0.75	1.35×10^{4}	1.11×10^{-5}	0.91
	8	13.93	49.61	5.88×10^{-5}	0.76	1.42×10^{4}	1.52×10^{-5}	0.85
	9	13.88	49.49	6.84×10^{-5}	0.75	1.46×10^{4}	7.11×10^{-6}	0.96
	10	13.80	54.62	6.71×10^{-5}	0.75	1.53×10^{4}	8.15×10^{-6}	0.95
0.2 mol/L NaOH 30 MPa	1	9.32	55.22	4.35×10^{-5}	0.79	838.52	2.58×10^{-5}	0.72
	2	9.42	58.41	2.82×10^{-5}	0.82	1218.73	1.77×10^{-5}	0.75
	3	9.61	69.97	2.58×10^{-5}	0.83	1681.29	1.18×10^{-5}	0.77
	4	9.58	71.44	2.29×10^{-5}	0.84	2031.22	1.10×10^{-5}	0.79
	5	9.68	75.14	2.27×10^{-5}	0.84	2558.70	9.21×10^{-6}	0.79
	6	9.68	81.56	2.10×10^{-5}	0.85	3006.00	9.14×10^{-6}	0.80
	7	9.95	74.14	2.11×10^{-5}	0.85	3630.10	9.26×10^{-6}	0.80
	8	9.79	80.07	1.97×10^{-5}	0.85	3964.79	8.34×10^{-6}	0.81
	9	9.85	81.72	1.90×10^{-5}	0.86	4559.48	8.29×10^{-6}	0.81
	10	9.85	92.82	1.16×10^{-5}	0.90	5490.90	7.85×10^{-6}	0.76
3.5% NaCl 0.1 MPa	1	12.57	12.50	1.21×10^{-4}	0.74	210.92	1.32×10^{-5}	0.85
	2	12.20	10.73	1.05×10^{-4}	0.75	204.21	3.44×10^{-5}	0.81
	3	12.23	9.13	1.08×10^{-4}	0.75	203.45	2.81×10^{-5}	0.85
	4	11.44	9.15	1.05×10^{-4}	0.75	191.57	3.45×10^{-5}	0.83
	5	11.42	8.26	1.03×10^{-4}	0.75	201.10	2.44×10^{-5}	0.87
	6	11.37	7.16	1.01×10^{-4}	0.75	207.42	2.82×10^{-5}	0.85
	7	11.50	6.27	1.08×10^{-4}	0.75	217.75	2.90×10^{-5}	0.85
	8	11.04	5.09	8.92×10^{-5}	0.76	210.10	3.40×10^{-5}	0.82
	9	11.38	5.60	7.33×10^{-5}	0.77	233.00	3.71×10^{-5}	0.79
	10	11.40	4.52	1.24×10^{-5}	0.77	247.83	7.79×10^{-5}	0.78
3.5% NaCl 30 MPa	1	9.42	6.00	3.72×10^{-6}	1	232.22	1.10×10^{-4}	0.73
	2	8.70	6.79	4.61×10^{-6}	0.98	226.55	8.39×10^{-5}	0.72
	3	8.11	9.02	6.56×10^{-6}	0.94	225.30	5.99×10^{-5}	0.72
	4	7.89	10.95	7.82×10^{-6}	0.92	221.87	5.09×10^{-5}	0.74
	5	8.02	12.28	1.13×10^{-5}	0.91	238.20	5.16×10^{-5}	0.75
	6	7.93	12.83	1.02×10^{-5}	0.90	238.62	4.36×10^{-5}	0.74
	7	8.03	13.52	1.08×10^{-5}	0.89	242.97	4.18×10^{-5}	0.74
	8	8.17	13.95	1.04×10^{-5}	0.90	253.33	3.90×10^{-5}	0.75
	9	8.32	16.43	1.25×10^{-5}	0.88	262.28	3.39×10^{-5}	0.76
	10	8.41	19.82	1.51×10^{-5}	0.80	270.26	2.79×10^{-5}	0.77
Artificial sea water 0.1 MPa	1	10.94	3.98	1.13×10^{-5}	0.88	101.18	1.70×10^{-4}	0.70
	2	12.39	4.48	1.45×10^{-5}	0.84	175.23	1.55×10^{-4}	0.70
	3	13.23	6.50	2.94×10^{-5}	0.76	213.53	1.20×10^{-4}	0.71
	4	15.76	6.49	1.82×10^{-5}	0.76	269.70	1.25×10^{-4}	0.70
	5	18.23	7.92	1.53×10^{-5}	0.74	305.12	1.30×10^{-4}	0.69
	6	15.38	7.79	2.70×10^{-5}	0.74	323.00	1.13×10^{-4}	0.72
	7	17.63	8.83	2.22×10^{-5}	0.72	368.69	1.19×10^{-4}	0.71
	8	18.54	9.27	2.14×10^{-5}	0.72	384.67	1.27×10^{-4}	0.71
	9	19.33	10.11	1.98×10^{-5}	0.71	419.73	1.22×10^{-4}	0.71
	10	19.81	10.34	1.92×10^{-5}	0.71	431.39	1.28×10^{-4}	0.70
Artificial sea water 30 MPa	1	7.15	8.85	3.59×10^{-5}	0.83	131.10	1.63×10^{-4}	0.70
	2	8.44	9.65	2.73×10^{-5}	0.87	184.92	1.65×10^{-4}	0.69
	3	9.08	11.85	2.37×10^{-5}	0.84	232.55	1.47×10^{-4}	0.69
	4	9.21	13.77	2.86×10^{-5}	0.79	269.57	1.03×10^{-4}	0.70
	5	9.59	14.07	1.22×10^{-5}	0.85	327.99	1.13×10^{-4}	0.70
	6	9.62	14.49	3.50×10^{-5}	0.77	365.44	7.85×10^{-5}	0.71
	7	9.77	16.04	3.63×10^{-5}	0.77	420.10	7.28×10^{-5}	0.71
	8	9.51	18.30	3.81×10^{-5}	0.76	435.80	6.94×10^{-5}	0.72
	9	10.10	19.81	3.39×10^{-5}	0.77	524.00	6.52×10^{-5}	0.72
	10	10.28	19.98	3.21×10^{-5}	0.78	552.86	6.48×10^{-5}	0.73

deposits that formed under 0.1 MPa, while only Mg was detected in the deposits that formed under 30 MPa. Barchiche et al. [24] and Héla et al. [28] claimed that brucite deposits were obtained when the cathodic potential was more negative than −1.3 V_{SCE} and the interfacial pH value was higher than 9.3 for steel in artificial seawater. However, brucite was detected under −1.2 V and 30 MPa in this experiment.

4. Discussion

4.1. Hydrostatic pressure effects on hydrogen permeation with cathodic deposits

The Tafel plots in Fig. 1 showed that the reaction on the hydrogen entry side was mainly controlled by the HER (reactions 1–5) at −1.2 V potential. With cathodic deposits on the specimens'

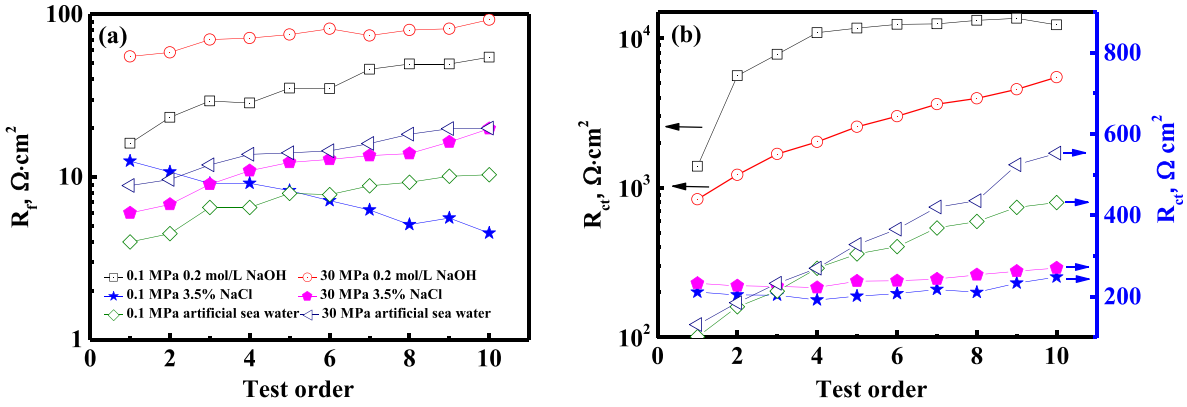

Fig. 5. Test order dependence of the R_f and R_{ct} values obtained by fitting the EIS data in Fig. 4 under various test conditions.

surface, the value of R_{ct} was related to HER, which occurs in the microscopic gaps between the deposits. The Faradic current, i_f, which is influenced by the HER, can be expressed as [7,12,29]:

$$i_f = -F(v_1 + v_2) \tag{9}$$

where F is the Faraday's constant and v_i is the reaction rate of the reaction (i), which can be represented as:

$$v_1 = k_1(1-\theta)\exp\left(\frac{-\alpha F\eta}{RT}\right) \tag{10}$$

$$v_2 = k_2\theta\exp\left(\frac{-\alpha F\eta}{RT}\right) \tag{11}$$

where k_i are the kinetic parameters of the reaction (i). α is the transfer coefficient, and η is the overpotential, while R and T are the

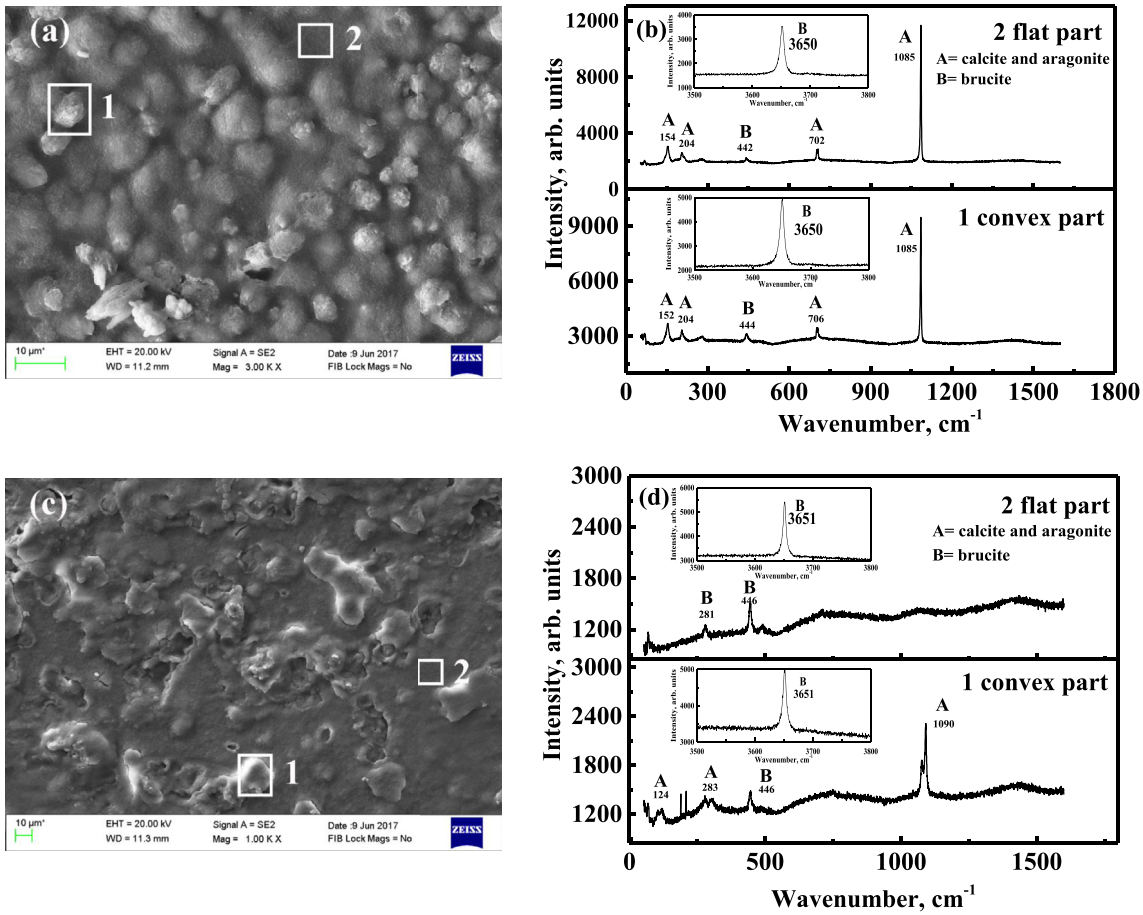

Fig. 6. SEM micrographs and the Raman spectra of the deposits formed at −1.2 V on the hydrogen entry side of A514 steel during hydrogen permeation in artificial seawater under different hydrostatic pressures. (a) and (b) are SEM micrographs and the Raman spectra under 0.1 MPa, respectively; (c) and (d) are SEM micrographs and the Raman spectra under 30 MPa, respectively.

gas constant and the absolute temperature, respectively. θ is the surface coverage of hydrogen atoms.

As mentioned in the introduction, hydrostatic pressure increased k_1 and k_2. Additionally, hydrostatic pressure increased the corrosion potential and caused η to be more negative. As found in a previously study, θ remained nearly constant under −1.2 V [12]. Thus, pressure increased the value of i_f and decreased the value of R_{ct} based on Eqs. (10) and (11). Additionally, pressure inhibited the recombination of hydrogen atoms in reaction (3) [11,12], inducing hydrogen permeation and increased permeation current density. These pressure effects were denoted as “pressure effect I”.

On the other hand, as mentioned above, hydrostatic pressure induced more hydrogen atoms to permeate into the specimens [11,12]. Thus, it can be reasonably assumed that more iron particles were disbanded from the specimens' surface and became iron ions under a relatively high hydrostatic pressure. Moreover, under a relatively high pressure, more OH^- were produced because of the increase of v_1 and v_2. Thus, hydrostatic pressure increased the production of cathodic deposits ($Fe(OH)_2$ or Fe(III) oxidation [14]). This effect decreased the area of the microscopic gaps in the deposits. Thus, the values of i_f and R_{ct} increased at higher hydrostatic pressure. Additionally, hydrogen entry and the permeation current density were inhibited by cathodic deposits. These pressure effects were denoted as “pressure effect II”. Under artificial seawater conditions, “pressure effect II” was more significant, since the cathodic deposits were denser. In conclusion, the R_{ct} value and permeation current density depend on both pressure effects I and II.

4.2. Hydrostatic pressure effects in 0.2 mol/L NaOH and 3.5% NaCl

According to Fig. 5, for the experiment in 0.2 mol/L NaOH, both R_f and R_{ct} increase with time. For 0.1 and 30 MPa, based on “pressure effect II”, hydrostatic pressure increased R_f because the production of the cathodic deposits increased. However, “pressure effect I” still controlled the permeation process, and the deposits did not obviously inhibit the hydrogen entry and HER. This conclusion can also be drawn from an examination of Fig. 2, which shows that the steady-state current density increased with pressure. Thus, hydrostatic pressure increases the occurrence of HER and decreases the R_{ct} value.

For the experiments in the 3.5% NaCl solution, it is found that the value of R_f decreased with time at 0.1 MPa, as shown in Fig. 5(a). Therefore, Cl^- inhibited the formation of $Fe(OH)_2$ or Fe(III) oxidation, as was shown by Sato [30]. Thus, the surface conditions remained nearly unchanged during the permeation. Additionally, the decrease in the permeation current density with permeation time was not as significant as in the 0.2 mol/L NaOH solution. However, this phenomenon was not observed at 30 MPa. Based on the “pressure effect II”, a 30 MPa hydrostatic pressure can induce denser cathodic deposits because more iron particles and OH^- groups are produced. It was found that the inhibition of Cl^- was

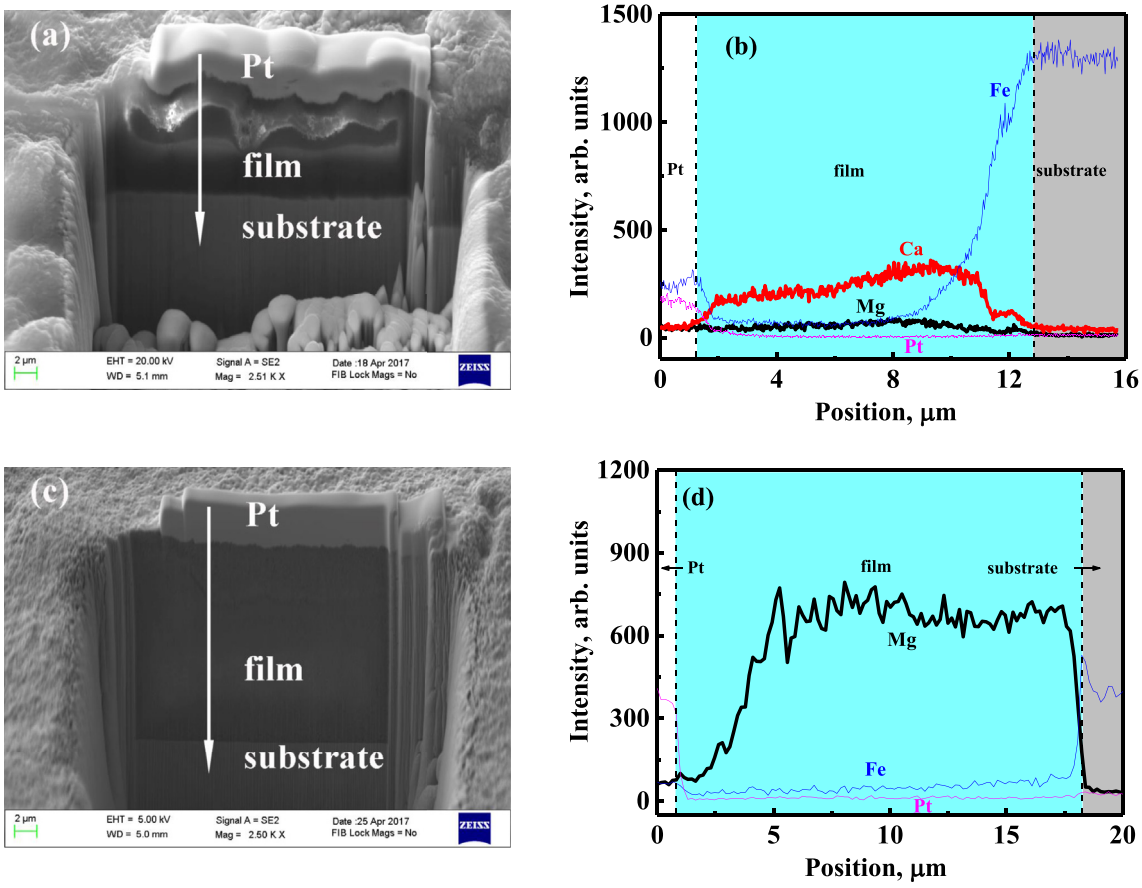

Fig. 7. Cross-sectional morphology and EDS line scan of deposits formed on the hydrogen entry side of A514 steel during hydrogen permeation in artificial seawater under different hydrostatic pressures. (a) and (b) Morphology and EDS line scan of deposits formed under 0.1 MPa, respectively; (c) and (d) Morphology and EDS line scan of deposits formed under 30 MPa, respectively.

more significant at 0.1 MPa than at 30 MPa.

4.3. Hydrostatic pressure effects in artificial seawater

As seen in Fig. 2, for the experiment in artificial seawater, the permeation current density decreased with hydrostatic pressure. Thus, the "pressure effect II" controlled the permeation process. Based on the fitting results shown in Fig. 5, the values of R_f and R_{ct} increased with hydrostatic pressure. Because pressure induced the generation of additional OH^- groups, according to reactions (1, 2) and Eqs. (10, 11), the interfacial pH increased with pressure. Once the interfacial pH reached 9.3, the deposits changed from $CaCO_3$ to $Mg(OH)_2$ [24], which explains why only $Mg(OH)_2$ was observed under −1.2 V at 30 MPa. Based on Fig. 7, the cathodic deposits formed at 30 MPa were thicker than at 0.1 MPa, decreasing the area of the microscopic gaps in the deposits. Thus, the value of R_{ct} increased with hydrostatic pressure.

It can be concluded that hydrostatic pressure increased the interfacial pH, which induced a change in the deposits from a mixture of brucite, aragonite, and calcite to brucite only. Pressure also increased the thickness of the deposits and inhibited hydrogen permeation into the specimen.

5. Conclusions

Hydrostatic pressure increased the interfacial pH and changed the deposits from a mixture of brucite, aragonite, and calcite to brucite only at −1.2 V in artificial seawater. This pressure effect controlled the permeation process (pressure effect II), thus increasing the pressure inhibited hydrogen permeation into the specimen.

However, since the deposits formed in 0.2 mol/L NaOH and 3.5% NaCl were very thin, hydrostatic pressure still induced the entry of hydrogen atoms (pressure effect I). Thus, hydrostatic pressure accelerates hydrogen permeation.

Acknowledgments

This project was supported by the National Nature Science Foundation of China under grant No. 51371035 and the National Basic Research Program of China under grant No. 2014CB643301.

References

[1] T.S. Taylor, T. Pendlington, R. Bird, Foinaven super duplex materials cracking investigation, in: Offshore Technology Conference, Houston, Texas, 10965, 1999.
[2] S.M. Hesjevik, Hydrogen embrittlement from cathodic protection on super-martensitic stainless steel – case history, Corrosion (04545) (2004).
[3] L. Nanis, J.J. DeLuccia, Effects of hydrostatic pressures on electrolytic hydrogen in iron, ASTM 445 (1969) 55–67.
[4] J. Woodward, R.P.M. Procter, The effect of hydrostatic pressure on hydrogen permeation and embrittlement of structural steels in seawater, Conf. Proc. (1996) 253–267.
[5] R.F. Blundy, L.L. Shreir, The effect of pressure on the permeation of hydrogen through steel, Corrosion Sci. 17 (1977) 509–527.
[6] A. Smirnova, R. Johnsen, Influence of temperature and hydrostatic pressure on hydrogen diffusivity and permeability in 13%Cr super martensitic stainless steel under cathodic protection, Corrosion (2010) 10292.
[7] L. Bai, D.A. Harrington, B.E. Conway, Behavior of overpotential—deposited species in Faradaic reactions—II. ac Impedance measurements on H2 evolution kinetics at activated and unactivated Pt cathodes, Electrochim. Acta 32 (1987) 1713–1731.
[8] A. Lasia, Applications of electrochemical impedance spectroscopy to hydrogen adsorption, evolution and absorption into metals, in: B. Conway, R. White (Eds.), Modern Aspects of Electrochemistry, Springer, US, 2002, pp. 1–49.
[9] D.A. Harrington, B.E. Conway, AC Impedance of Faradaic reactions involving electrosorbed intermediates—I. Kinetic theory, Electrochim. Acta 32 (1987) 1703–1712.
[10] T.Y. Zhang, Y.P. Zheng, Effects of absorption and desorption on hydrogen permeation—I. Theoretical modeling and room temperature verification, Acta Mater. 46 (1998) 5023–5033.
[11] X.L. Xiong, X. Tao, Q.J. Zhou, J.X. Li, A.A. Volinsky, Y.J. Su, Hydrostatic pressure effects on hydrogen permeation in A514 steel during galvanostatic hydrogen charging, Corrosion Sci. 112 (2016) 86–93.
[12] X.L. Xiong, Q.J. Zhou, J.X. Li, A.A. Volinsky, Y.J. Su, Cathodic over-potential and hydrogen partial pressure coupling in hydrogen evolution reaction of marine steel under hydrostatic pressure, Electrochim. Acta 247 (2017) 1019–1029.
[13] X.L. Xiong, H.X. Ma, X. Tao, J.X. Li, Y.J. Su, Q.J. Zhou, A.A. Volinsky, Hydrostatic pressure effects on the kinetic parameters of hydrogen evolution and permeation in Armco iron, Electrochim. Acta 255 (2017) 230–238.
[14] T. Zakroczymski, J. Flis, Impedance characterization of the activation of iron surface for hydrogen entry from alkaline solution, Electrochim. Acta 41 (1996) 1245–1250.
[15] H.L. Goff, Use of Raman spectroscopy and rotating split ring disk electrode for identification of surface layers on Iron in 1M NaOH, J. Electrochem. Soc. 137 (1990) 2684–2690.
[16] J. Flis, H. Oranowska, Z. Szklarska-Smialowska, An ellipsometric study of surface films grown on iron and iron-carbon alloys in 0.05 M KOH, Corrosion Sci. 30 (1990) 1085–1099.
[17] A. Gajek, T. Zakroczymski, Long-lasting hydrogen evolution on and hydrogen entry into iron in an aqueous solution, J. Electroanal. Chem. 578 (2005) 171–182.
[18] C. Deslouis, D. Festy, O. Gil, V. Maillot, S. Touzain, B. Tribollet, Characterization of calcareous deposits in artificial sea water by impedances techniques: 2-deposit of $Mg(OH)_2$ without $CaCO_3$, Electrochim. Acta 45 (2000) 1837–1845.
[19] Z. Gao, Effect of Calcareous Sediments on Hydrogen Evolution Potential of 16Mn Steel in Seawater, 2016, pp. 3007–3023.
[20] T. Okstad, Ø. Rannestad, R. Johnsen, K. Nisancioglu, Significance of hydrogen evolution during cathodic protection of carbon steel in seawater, Corrosion 63 (2007) 857–865.
[21] X.L. Xiong, Q.J. Zhou, J.X. Li, A.A. Volinsky, Y.J. Su, Corrigendum to "Cathodic over-potential and hydrogen partial pressure coupling in hydrogen evolution reaction of marine steel under hydrostatic pressure", Electrochim. Acta 247C (2017) 1019–1029.
[22] C. Deslouis, I. Frateur, G. Maurin, B. Tribollet, Interfacial pH measurement during the reduction of dissolved oxygen in a submerged impinging jet cell, J. Appl. Electrochem. 27 (1997) 482–492.
[23] C. Deslouis, D. Festy, O. Gil, G. Rius, S. Touzain, B. Tribollet, Characterization of calcareous deposits in artificial sea water by impedance techniques—I. Deposit of $CaCO_3$ without $Mg(OH)_2$, Electrochim. Acta 43 (1998) 1891–1901.
[24] C. Barchiche, C. Deslouis, D. Festy, O. Gil, P. Refait, S. Touzain, B. Tribollet, Characterization of calcareous deposits in artificial seawater by impedance techniques: 3—deposit of $CaCO_3$ in the presence of Mg(II), Electrochim. Acta 48 (2003) 1645–1654.
[25] H. Addach, P. Berçot, M. Rezrazi, M. Wery, Hydrogen permeation in iron at different temperatures, Mater. Lett. 59 (2005) 1347–1351.
[26] C. Barchiche, C. Deslouis, O. Gil, P. Refait, B. Tribollet, Characterisation of calcareous deposits by electrochemical methods: role of sulphates, calcium concentration and temperature, Electrochim. Acta 49 (2004) 2833–2839.
[27] ASTM-D1141-98, Standard Practice for the Preparation of Substitute Ocean Water, Annual Book of ASTM Standards, American Society for Testing and Materials, Philadelphia, Pennsylvania, USA, 2004.
[28] H. Karoui, B. Riffault, M. Jeannin, A. Kahoul, O. Gil, M.B. Amor, M.M. Tlili, Electrochemical scaling of stainless steel in artificial seawater: role of experimental conditions on $CaCO_3$ and $Mg(OH)_2$ formation, Desalination 311 (2013) 234–240.
[29] C. Lim, S.-I. Pyun, Theoretical approach to Faradaic admittance of hydrogen absorption reaction on metal membrane electrode, Electrochim. Acta 38 (1993) 2645–2652.
[30] N. Sato, Whitney Award Lecture: toward a more fundamental understanding of corrosion processes, Corrosion 45 (1989) 354–368.